Volume 13
Number 9
7 March 2025
Pages 6107–6848

Journal of Materials Chemistry A

Materials for energy and sustainability

rsc.li/materials-a

ISSN 2050-7488

ROYAL SOCIETY OF CHEMISTRY

PERSPECTIVE

Morgan Stefik *et al.*

Capacity-weighted figures-of-merit for battery transport metrics

Journal of Materials Chemistry A

ROYAL SOCIETY OF CHEMISTRY

PERSPECTIVE

View Article Online
View Journal | View Issue

Cite this: J. Mater. Chem. A, 2025, 13, 6314

Capacity-weighted figures-of-merit for battery transport metrics†

CJ Sturgill, [a] Christopher Sutton, [a] Julian Schwenzel [b] and Morgan Stefik *[a]

New battery materials with improved transport are needed. Typical measurements yield widely varying voltage-dependent diffusivities and reporting practices are diverse. Some materials (*e.g.* first-order phase change) have most redox occur at a specific voltage and may be sufficiently represented by singular transport metrics. Many rapid intercalation materials, however, exhibit second-order phase transitions with redox over a broad voltage range. How should such cases be compared? The use of capacity-weighted average values is suggested where voltage-dependent metrics are consolidated into representative descriptors as figures-of-merit. Examples are elaborated where differential capacity (dQ/dV) is used to derive a weighting function to calculate a diffusivity figure-of-merit (D_{Qav}). Furthermore, it is shown that galvanostatic techniques can provide transport values with even capacity-weighting such that their mean value (D_{Tav}) is capacity-weighted. Though equivalent conceptually, the latter approach avoids derivative noise and subjective smoothing. Computational diffusion values can similarly include capacity-weighted figures-of-merit. Lastly, diffusivity uncertainty is addressed which is dominated by surface area error due to the second-power dependence. Best-practices can reduce the diffusivity error from ~40% to ~2% using appropriate BET sorbents or SAXS with thickness measurements. These perspectives improve the comparison of battery materials with a diffusivity figure-of-merit that supports performance-ranking with attention to uncertainty.

Received 26th August 2024
Accepted 18th December 2024

DOI: 10.1039/d4ta06041e

rsc.li/materials-a

Introduction

Battery publications have rapidly increased over the past 20 years with a plethora of new materials with improved transport characteristics.[1] Battery performance is ultimately linked to the ionic and electronic transport characteristics of the active materials used.[2,3] While there is considerable tunability *via* electrode optimizations (additives, particle size, thickness, porosity) these often come with tradeoffs.[4] Volume used for components other than active material necessarily lower the cell-level energy density. Thus, there are benefits with active materials that have improved ionic and/or electronic transport characteristics which require less downsizing and a smaller fraction of non-active materials to reach performance targets. Figures-of-merit (FOM) are representative metrics that are intended to quantitatively rank a given attribute. FOMs such as ionic diffusivity are important for comparing materials directly without the additional convolved effects of the electrode architecture.[5,6] Diffusivity values are readily measured with techniques such as intermittent current interruption (ICI),[7,8] galvanostatic intermittent titration technique (GITT),[9,10] potentiostatic intermittent titration technique (PITT),[11,12] and electrochemical impedance spectroscopy (EIS).[13,14] These techniques are generally used to measure voltage-dependent diffusivity values across a voltage range with varying state-of-charge (SOC) (Fig. 1a).[15] The resulting diffusivity values can vary by an order of magnitude or more for a given material as a function on the voltage/SOC. Please note that first order phase change materials have a single voltage when two phases are present under equilibrium as expressed in Gibb's Phase Rule. Rather here we focus on second order phase change materials where the equilibrium potential of the single phase depends solely upon the SOC. The relative ranking of different materials is simple when one sample exhibits higher diffusivity across the whole voltage range. In contrast, comparing samples with intersecting diffusivities requires additional consideration.

The ranking of sample diffusivities is enabled by using a representative FOM. There is not, however, universal agreeance in the literature for how to rank materials in terms of diffusivity. Some publications emphasize maximum diffusivity values[16,17] while others focus on specific SOCs[18,19] or the voltage(s) of maximum differential capacity (dQ/dV).[20,21] A FOM must be representative of overall sample performance. First-order phase change materials exhibit a voltage plateau with a corresponding sharp peak in differential capacity (Fig. 1b and d).[22,23] The diffusivity value corresponding to this principal voltage may be

[a]Department of Chemistry and Biochemistry, University of South Carolina, Columbia, SC 29201, USA. E-mail: morgan@stefikgroup.com

[b]Fraunhofer Institute of Advanced Manufacturing Technology and Advanced Materials IFAM, Wiener Strasse 12, 28359 Bremen, Germany

† Electronic supplementary information (ESI) available. See DOI: https://doi.org/10.1039/d4ta06041e

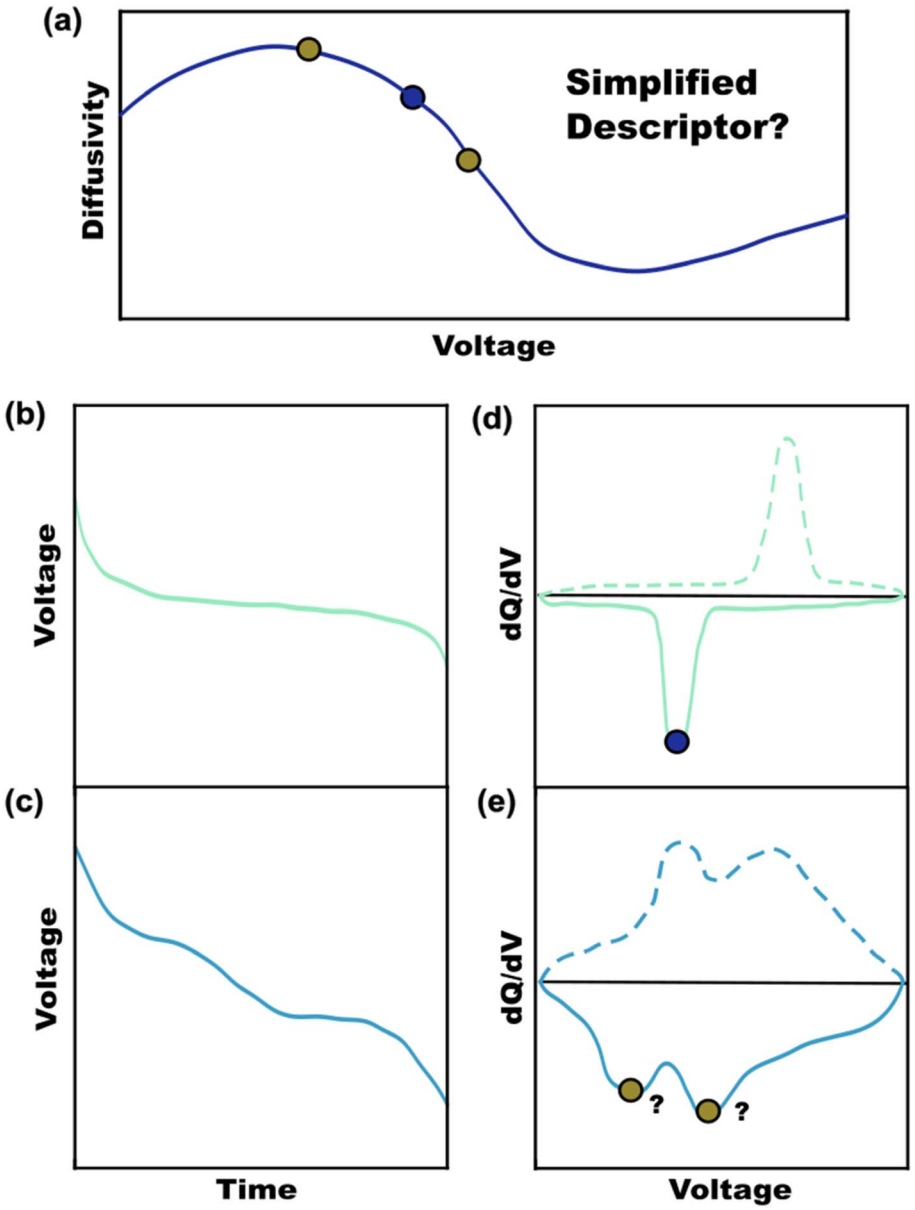

Fig. 1 Conceptual scheme showing (a) diffusivity as a function of voltage (arbitrary shape selected). One convention for reporting diffusivity is to examine the (b) lithiation voltage profile and the corresponding ((d), solid line) differential capacity plot to report the single diffusivity value at the point of maximum charge transfer (blue dot). It is less clear how one should compare *e.g.* (c and e) samples with second-order phase transitions which exhibit charge transfer over a wide voltage range and can have multiple peaks (yellow circles). There is a need for a better descriptor as a figure-of-merit that goes beyond lone-points to capture a broader perspective while facilitating simple sample ranking.

a sufficient FOM for such first-order samples, though it may not be clear how each phase contributes towards diffusion. A range of rapid-intercalation materials exhibit second-order phase transitions where diffusivity FOMs are particularly elusive. Such second-order materials do not phase separate during lithiation, but rather exhibit a continuum of lattice distortions. This feature can enable improved longevity by limiting cracking and minimizes voltage hysteresis by avoiding first-order phase transitions.[24] Example second-order materials include T-Nb_2O_5 (ref. 24 and 25) and a range of Wadsley–Roth niobates such as $TiNb_2O_7$,[6,26–29] $Nb_{16}W_5O_{55}$,[30,31] and $MoNb_{12}O_{33}$ (ref. 32 and 33) to name a few. Some intercalation materials also transition from first-order to second-order behavior with downscaling the particle sizes.[34,35] Regardless of the type of phase change, it is prudent to use near-equilibrium conditions (low enough current densities) for diffusion measurements to avoid deviations that depend on the electrode structure. Second-order transitions tend to be associated with a sloped voltage profile (not a plateau) where the corresponding differential capacity plot has broad features, sometimes with multiple peaks and a non-zero baseline (Fig. 1c and e).[22,23] Varying crystallinity in battery materials can also influence broadening with charge storage, making a single voltage no longer representative.[6,36,37] In these cases, selecting a single diffusivity value would generally fail to account for the

full range of behaviors exhibited during battery usage. Complete voltage-dependent profiles benefit battery simulations but are inconvenient as a FOM for ranking materials. A suitable FOM should derive a single value that reflects the full range of voltage-dependent diffusivity values with an appropriate weighting for the relative importance of each measured value.

Capacity-weighted figures-of-merit

A capacity-weighted average diffusivity is suggested in this perspective where the collection of voltage-dependent diffusivities are consolidated into a single descriptor as a representative FOM. Intercalation materials with second-order transitions in particular need a better diffusivity FOM since they exhibit a continuum of lattice configurations during lithiation, each with different diffusivity values. Capacity-weighting here is intended to scale each measured diffusivity value in proportion to its relative contribution towards the total charge stored. In this way, dominant redox features (dQ/dV peaks) have higher weighting than minor redox features (dQ/dV shoulders) when combining voltage-dependent diffusivities. Naturally this data reduction involves information loss with the benefit that the resulting FOM enables simple ranking of materials in a more wholistic and non-arbitrary way. One benefit of such a weighted average is that the resulting FOM preserves the same units and magnitude as the complete dataset. Two approaches will be elaborated in the next sections with different numerical methods for implementing such capacity-weighted average diffusivities.

A material's differential capacity (dQ/dV) can be used to derive a capacity-weighting function to evaluate an average

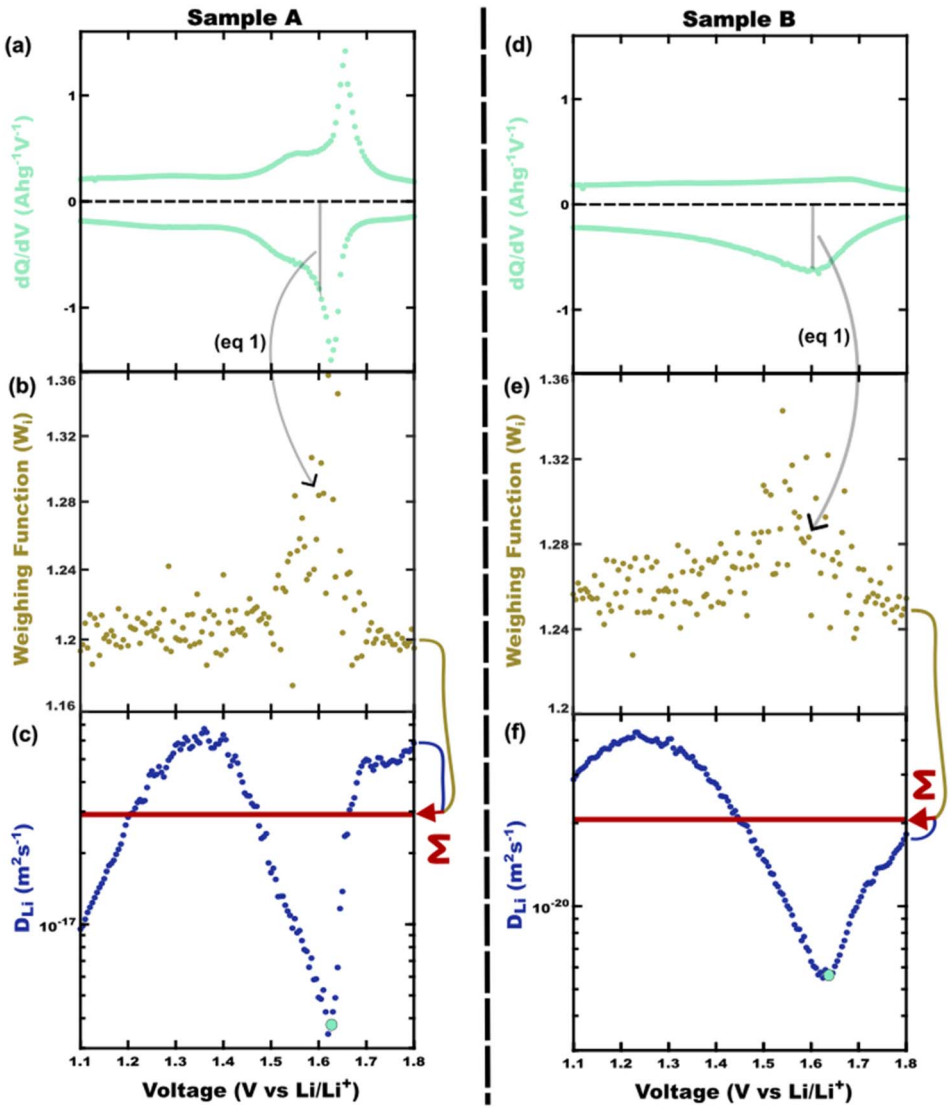

Fig. 2 The differential capacity can be combined with the complete set of diffusivity values to derive a representative descriptor. Two examples are presented (Samples A and B) side-by-side. Each point on the (a and d) dQ/dV plot yields a capacity-weighting term (gray shaded area, eqn (1)). Each (b and e) weight value, $W_i(V)$, is multiplied by the respective diffusivity value, $D_i(V)$, (c and f) and summed (red arrow) to yield the capacity-weighted diffusivity (D_{Qav}) as a figure-of-merit (red line). In both these cases, the diffusivity at peak dQ/dV (D_{QP}, green dot) is quite different from the more complete D_{Qav} descriptor.

diffusivity FOM. This method scales each measured diffusivity value according to the incremental amount of charge passed (both are voltage-dependent) to weight all diffusivity values according to their relative contribution towards overall charge storage. Two samples are presented conceptually using this approach: a fully-crystalline Sample A and a defect-rich crystalline Sample B.[6] Example data will be considered for a well-known intercalation material that exhibits second-order phase changes upon lithiation, $TiNb_2O_7$. The sample details are irrelevant for the FOM discussion; however, the presented $TiNb_2O_7$ samples were annealed at 1100 °C and 700 °C. The differential capacity plots indicate distinctly different trends of charge storage as a function of voltage (Fig. 2a and d). The corresponding ICI derived diffusivity values as a function of voltage are shown in Fig. 2c and f. Despite both samples having a peak of differential capacity, both samples also have a significant fraction of charge storage spread across the entire voltage range measured. It follows that the diffusivity values for all of these voltages would be overlooked if reporting diffusivity from a single-voltage alone. The capacity-weighting terms (W_i) for the i-ith voltage are calculated as the piecewise integrals under the dQ/dV curve as scaled by the full integral:

$$w_i = \frac{\int_{V_i}^{V_{i+1}} \frac{dQ}{dV} dV}{\int \frac{dQ}{dV} dV} \quad (1)$$

In this way the total sum of all weighting terms is 1.00 (100%) to preserve the magnitude of the weighted average (analogous to a probability distribution function). An example integral is shaded (Fig. 2a and d) with the corresponding weighting term shown in Fig. 2b and e. The sum of the weighted diffusivities (Fig. 2c and f red line) corresponds to the capacity-weighted average FOM (D_{Qav}):

$$D_{Qav} = \sum_i w_i D_i \quad (2)$$

Comparing the diffusivity values of Sample A at the voltage of peak charge storage (D_{Qp}, Fig. 2c and f green dots) to the D_{Qav} reveals an 87% error with the single-point reporting approaches. This comparison highlights the amount of information missed when reporting diffusivity values from second-order materials measured at a single-voltage. Derivative calculations such as dQ/dV naturally amplify the noise of the underlying galvanostatic data. It is typical for dQ/dV plots to require curve smoothing which can bring a subjective component to the numerical analysis (ESI Fig. S2†). Furthermore, the data coordinates along the voltage axis can differ between the dQ/dV values and the ICI diffusivity values, requiring interpolation and the associated error when aligning the voltage coordinates. Thus, transforming dQ/dV into a weighting function enables the calculation of a capacity-weighted average

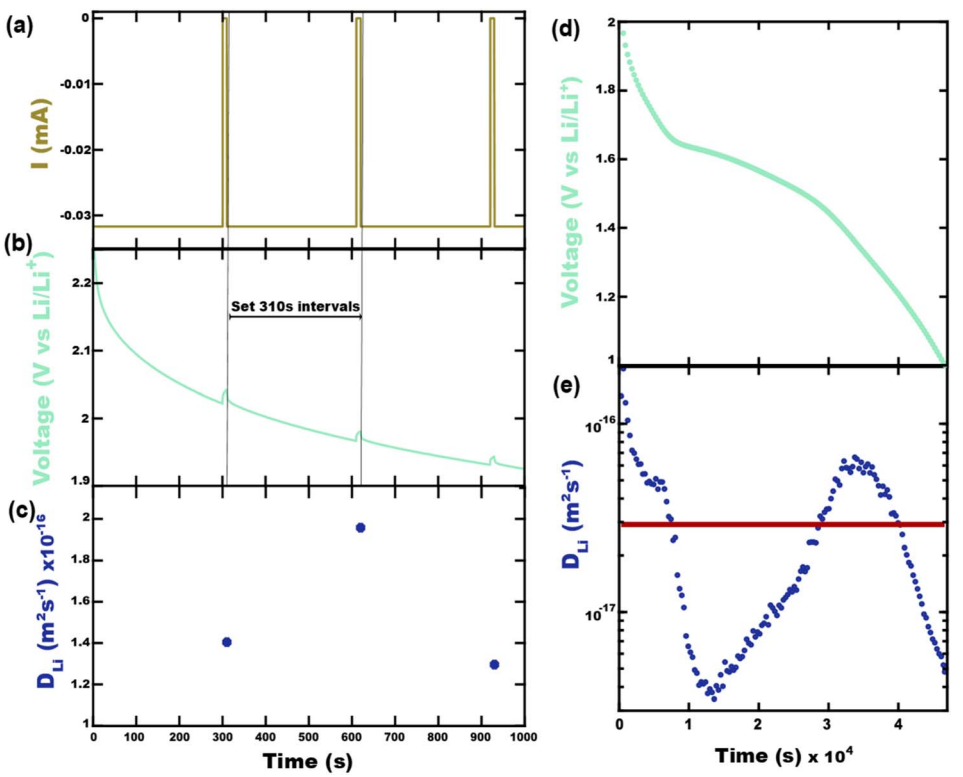

Fig. 3 Capacity-weighting can also be accomplished with time-averaged values from galvanostatic measurements such as GITT/ICI. The fixed galvanostatic/interruption time intervals of the ICI method vary (a) current and (b) voltage repeatedly for each (c) diffusivity value. A complete measurement spans the (d) voltage window to produce a set of (e) diffusivity values. Such galvanostatic measurements (constant current) with constant time intervals naturally measure values spaced with constant intervals of capacity. The mean value of this time-spaced set of diffusivity values (D_{Tav}, red line) is thus capacity-weighted. The presented values correspond to Sample A.

diffusivity with the possibility of requiring subjective curve smoothing and interpolation.

It will be shown that galvanostatic measurements of diffusivity values (ICI/GITT) naturally yield values that are evenly weighted in terms of capacity. In contrast to voltage-controlled methods such as PITT, galvanostatic measurements are carried out with current-control. ICI, for example, typically employs a constant current for a fixed duration in between temporary interruptions to open circuit conditions (Fig. 3a). The voltage is measured continuously throughout ICI measurements to derive the pseudo-open-circuit-potential, resistance, diffusion resistance, and diffusivity (Fig. 3b), *vide infra*. These four values are evaluated once for each transient interruption (Fig. 3c) where the complete measurement contains numerous evaluated points in time (Fig. 3d and e). Given that ICI uses a constant current with fixed time intervals there is the same amount of charge passed between each interruption stage. From this perspective, all measured values are evenly capacity-weighted. Table 1 clarifies this mathematical fact using Sample A with the first three interruptions enumerated. Here the fixed interval of ΔQ between time-samples is apparent despite the varying $\Delta Q/\Delta V$ and ΔV values. Since the values are evenly capacity-weighted in this fashion, a mean value (D_{Tav}, "time-averaged") is also capacity-weighted (Table 1 and Fig. 3e red line):

$$D_{\mathrm{Tav}} = \overline{D_i} \tag{3}$$

where D_i is each calculated diffusivity value with constant increments of capacity. Again, comparing this FOM to the diffusivity measured at peak differential capacity leads to 87% error for the single-point value. Thus, two mathematically equivalent methods of calculating capacity-weighted average diffusivity were presented. Please note that in the limit of infinite instrumental resolution these two methods are mathematically equal:

$$\lim_{i\to\infty} D_{\mathrm{Qav}} = \lim_{i\to\infty} D_{\mathrm{Tav}} \tag{4}$$

Rather, the differences between D_{Qav} and D_{Tav} in practice are in their numerical evaluation. The calculation of D_{Qav} using $\mathrm{d}Q/\mathrm{d}V$ values involves derivative noise and subjective curve smoothing. In contrast, the calculation of D_{Tav} does not involve subjective factors but does require the use of ICI/GITT.

These two numerical methods are next compared to values from the peaks in differential capacity. Fig. 4a compares three different methods of presenting diffusivity values. Both D_{Qav} and D_{Tav} are closely related by both employing capacity-weighting but are different in terms of the numerical methods. Their corresponding values are nearly identical with 0.69% difference for the presented Sample A datasets. It is noteworthy that using $\mathrm{d}Q/\mathrm{d}V$ derived from the ICI data would yield the exact same result as time averaging (Fig. S1,† $D_{\mathrm{Qav}} = D_{\mathrm{Tav}}$). As pointed out above, the use of D_{Qp} disregards most of the measured diffusivity values and is inherently a less representative value for intercalation materials with second-order phase transitions (Fig. 4a). Extending this concept further, the same sort of capacity-weighted averages can be determined for other ICI/GITT metrics such as the diffusion resistance (K) or cell resistance (R) (Table 1 and Fig. 4b). Analogously capacity-weighted values of ionic conductivity or electrical conductance could similarly be calculated. We argue that using representative FOMs is important when comparing existing and newly discovered battery materials that exhibit second order phase transitions.

Computational diffusivity

Analogous to experimental reporting of diffusivity noted above, it is important that computational simulations also include a range of SOCs for second-order phase change materials to derive descriptors that are representative of overall performance. Here capacity-weighted diffusivities can be calculated using eqn (3) when numerous diffusivity values are calculated with evenly spaced lithium stoichiometries. Recent mechanistic studies of Nb-based Wadsley–Roth materials have highlighted the role of local and long-range structural changes during lithium insertion.[38,39] There are broadly two computational methods for diffusion analysis: (1) the calculation of activation energies for specific microscopic pathways and (2) molecular dynamics to derive the mean-squared displacement. Calculating activation energies with *e.g.* nudged elastic band (NEB) requires first identifying the lowest energy Li–interstitial sites *via* enumeration of all possible configurations. In the case of such Wadsley–Roth structures, this appears limited to low

Table 1 Tabulated values showing how the calculation of D_{Tav} is a capacity-weighted average. Data are recorded over fixed time intervals, each with corresponding values for time, charge, voltage and the associated model-based calculations of diffusivity, diffusion resistance, and resistance. The combination of galvanostatic conditions with fixed time intervals leads to constant ΔQ values and thus even capacity-weighting for each time point measured. Table sums correspond to the measurement time, voltage change, capacity, and a sum of 1.00 for weighting terms. The corresponding mean values ("time averaged") for diffusivity, resistance, and diffusion resistance are thus each capacity-weighted. The presented values correspond to Sample A

Intervals	1	2	3	—	Sum	Mean
Δt (s)	310	310	310	—	4.66×10^{4}	—
$\Delta Q/\Delta V$ (mA h g^{-1} V^{-1})	8.32	26.9	41.7	—	3.47×10^{4}	—
ΔV (V)	2.33×10^{-1}	7.20×10^{-2}	4.65×10^{-2}	—	1.90	—
ΔQ (mA h g^{-1})	1.94	1.94	1.94	—	291	—
Weight	6.67×10^{-3}	6.67×10^{-3}	6.67×10^{-3}	—	1.00	—
Diffusivity (m^2 s^{-1})	1.40×10^{-16}	1.96×10^{-16}	1.30×10^{-16}	—	—	2.92×10^{-17}
Cell resistance (Ω)	238	176	150	—	—	87.9
Diffusion resistance (Ω $s^{-0.5}$)	133	91.7	76.5	—	—	38.5

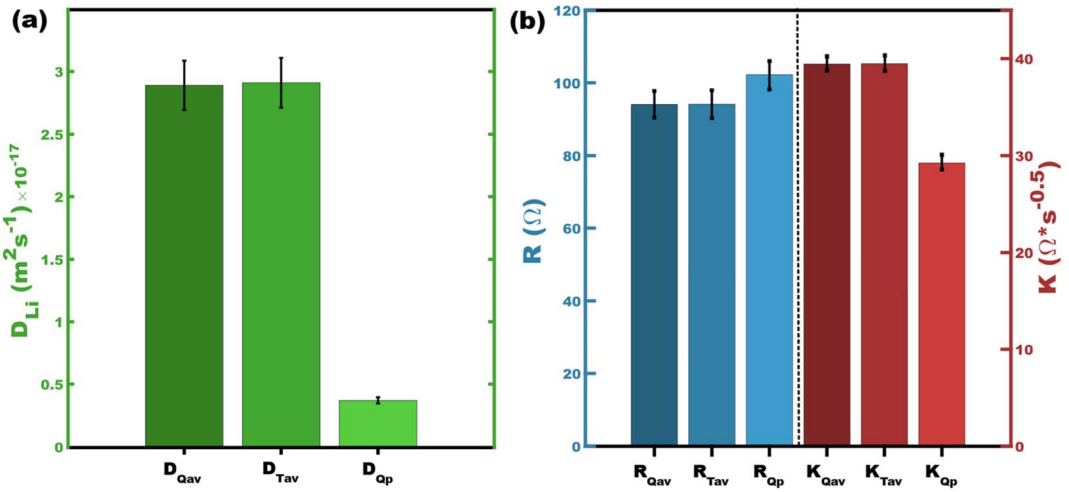

Fig. 4 Comparisons of (a) diffusivity, (b) resistance, and (b) diffusion resistance figures-of-merit based on capacity-weighting from dQ/dV ("Qav"), time-averaged ("Tav"), and charge peak ("Qp") methods. The Qav and Tav methods are conceptually equivalent but vary in numerical methods. Data correspond to Sample A.

lithium concentrations due to the combinatorial expansion of the calculations with higher SOCs. Regarding the second route, *ab initio* Molecular Dynamics (AIMD) simulations can calculate lithium dynamics explicitly over a range of concentrations. With AIMD simulations of structures with a wide range of activation energies (*e.g.* Wadsley–Roth structures) the selection of simulation temperature is crucial to enable all relevant pathways within the simulated timeframe.[39] The resulting AIMD diffusivity values can be scaled to the experimental temperature using the Einstein relationship.[40] Doing this analysis over a wide ranging SOCs is challenging due to the number of equivalent configurations and the computational cost of DFT. A simplified way to address the SOC phase transitions is by first determining the relevant short-range configurational order using cluster expansion and preserve that in AIMD simulations. Furthermore, machine learning potentials (MLPs) can bypass the need for running DFT within MD simulations. This accelerates the MLP-based AIMD calculations by orders of magnitude without sacrificing accuracy. Notably there are available foundation models (MACE-MP0, CHGNet, and M3GNet)[41–43] that can be used "out of the box" without training or fine-tuning. A broader, long-term challenge for computational simulations is addressing long-range diffusion including complications such as structural heterogeneity and crystalline defects such as grain/phase boundaries, point defects, and stacking faults. This is a grand challenge for computational approaches to identify preferred configurations amongst a many-parameter landscape and then significantly expand the number of atoms and compute-time. Regardless of future improvements, existing computational techniques can be used to calculate capacity-weighted diffusivities.

Uncertainty considerations

The minimization of uncertainty is essential when comparing FOMs. Diffusivity calculations such as ICI/GITT/PITT/EIS all combine an electrochemical response time (s) with the diffusion length (m) to derive the $m^2\ s^{-1}$ units of diffusivity; correspondingly, all diffusivity calculations have these two inputs as sources of error. The time constant here is determined by a potentiostat, often with much less than a single percent of error (~0.1%) for the response time.[44] In contrast, the diffusion length measurement not only typically has the largest percent error but also has an outsized effect on the diffusivity uncertainty owing to its second-power dependance.[45,46] This squaring of the diffusion length in eqn (5) doubles the resulting percent error in the reported diffusivity value. For the sake of alignment with popular gas physisorption reporting, the diffusion length is often parameterized into diffusivity calculations *via* the mass-specific surface area (A). For example, the ICI method calculates each diffusivity value (D) as:

$$D = \frac{4}{\pi}\left(\frac{V}{A}\times\frac{\frac{\Delta E_{OC}}{\Delta t_1}}{\frac{dE}{dt^{0.5}}}\right)^2 \quad (5)$$

where V is the molar volume of the electrode material, E_{OC} is the open circuit potential, Δt_1 is the period of constant current applied between OCP measurements, E is the potential of the electrode, and t is the step time.[7] Please note that this established and widely utilized relationship assumes semi-infinite diffusion into a planar solid where model-challenges of finite size effects, non-planar geometry effects, inter-particle heterogeneity, or transient complexities are reviewed elsewhere outside the scope of this manuscript.[45] With the minimization of error in the A value being critical, attention is next turned to modern best-practices *via* gas physisorption and then X-ray scattering methods in turn.

The Brunauer–Emmett–Teller (BET) method of analysis for sample surface area by gas physisorption are commonplace. The possible sources of error include the sorbent selection, the model, and the analysis. It is becoming increasingly known that

N_2 as a physisorption gas can lead to ~20% error[47–49] in sample surface area due to its quadrupole moment which would correspond to ~40% error in the derived diffusivity metrics. In contrast, Ar as a sorbent has a spherical geometry, an ability to access smaller micropores, and no quadrupole moment which enables Ar BET to often have ~0.6% error.[47,48,50] This improved accuracy with Ar BET corresponds to ~1.2% error in the resulting diffusivity values which is sufficiently accurate for meaningful ranking. It should be noted that model and analysis error can also be substantial where a recent round robin study with 61 labs analyzing the same 18 isotherms led to 7.1–31% difference in the interpreted surface areas.[49] A challenge with BET measurements for batteries is the general need for ~1 m^2 of sample surface area which for micron scale particles with ~1 m^2 g^{-1} of specific surface area corresponds to significant ~1 gram quantity of sample. Furthermore, BET analysis typically

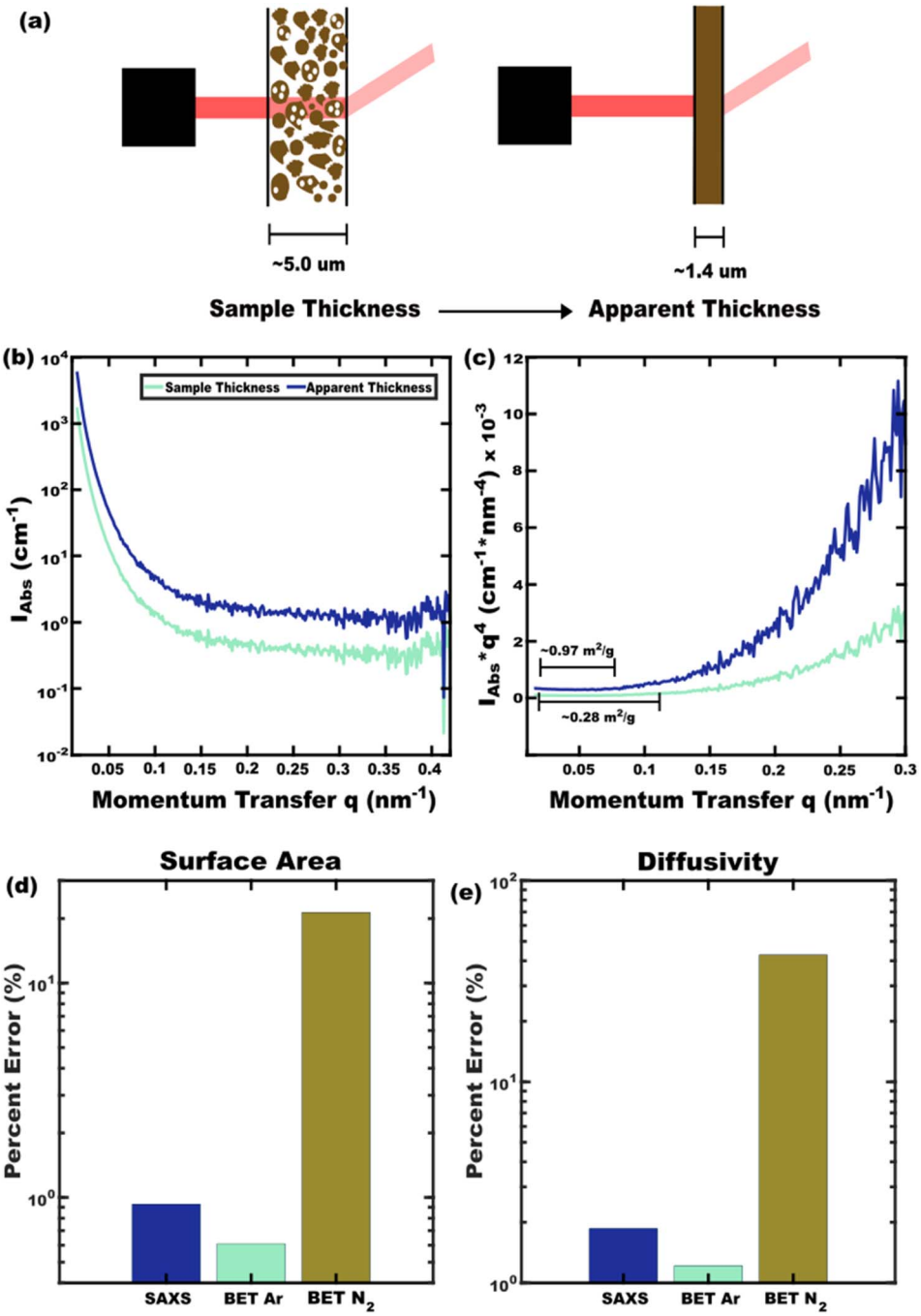

Fig. 5 SAXS analysis with (b) absolute scattering intensity can yield specific surface area when analyzing the (c) Porod region of a Porod plot. Here a typical (a) large source of error is the use of measured sample thickness rather than the more accurate effective sample thickness determined by X-ray transmission. Similarly, N_2 BET leads to significant (d) error in specific surface area whereas Ar BET or SAXS can be more accurate. The propagation of this error (e) to diffusivity values is important to consider when ranking materials. Nominal error values all obtained from ref. 48.

takes one to two days for sample degassing and subsequent analysis. Thus, BET with Ar gas is a best-practice method capable of enabling accurate diffusivity calculations.

Best-practices of Porod analysis of X-ray scattering data can also yield similarly accurate specific surface area measurements from few hr measurements on milligram sample quantities. In brief, here small-angle X-ray scattering (SAXS) data are acquired with absolute intensity units and background subtraction where analysis of the Porod region ($q_{\text{Porod}} > q_{\text{Fourier}}$) contains information about the sample surface.[51,52] It is important to note that calculating absolute intensity units requires accurate measurement of the beam brightness, the scattered intensity, and the sample thickness. A Porod plot is typically used ($I_{\text{abs}}q^4$ *vs.* q) where the constant value of $I_{\text{abs}}q^4$ in the high-q limit corresponds to the surface area to volume ratio (Σ):[53]

$$\Sigma = \frac{\lim_{q\to\infty}(I_{\text{abs}}q^4)}{2\pi(\Delta\text{SLD})^2} \quad (6)$$

The sample's scattering length density relative to vacuum (ΔSLD) can be determined using an online NIST calculator based on atomic scattering factors.[54] The Σ value can then be used to calculate the mass specific surface area (S):

$$S = \frac{\Sigma}{\rho} \quad (7)$$

where ρ is the bulk material density.[51] Please note that S in eqn (7) is identical to A in eqn (5) ($S = A$) where each equation was presented in its originally published form. From a perspective of uncertainty minimization, the inclusion of numerous $\Sigma(q)$ points within the Porod region improves the error-of-the-mean substantially where ~1% error is often achievable. The largest source of uncertainty with SAXS surface area measurements is otherwise the calibration of absolute scattering intensity. Here the unknown sample packing factor and the challenge of sample thickness measurement with calipers are best avoided as eloquently resolved by Spalla *et al.*[51,52] Here the best-practice is to calculate the apparent sample thickness based on the transmitted X-ray intensity using the linear attenuation coefficient (μ) available from a NIST online calculator.[55] The benefit of using the apparent thickness to determine absolute intensities is shown in Fig. 5a where there is a 4× difference in the derived specific surface area (Fig. 5b and c) when using this best practice as compared to using mechanical calipers. Please note that the apparent sample thickness of the SAXS sample is unrelated to the diffusion length. SAXS has convenience advantages for high-throughput screening since analysis does not require heated sample degassing and measurements can be carried out with just ~10 mg of sample. Such measurements can be completed in a few hrs at typical labscale SAXS facilities, many of which offer mail-in analysis.[56–60]

The diffusion length has also been measured with a diversity of other methods such as electron microscopy.[21] Electron microscopy has the benefit of being model-free, however care must be taken to avoid detection bias, human bias, and to include frequent instrument calibration with NIST standards under the same imaging conditions. Furthermore, being a localized measurement, the best-practice with microscopy also requires an abundance of measurements to calculate the average diffusion length (minimum radius) with minimal error-of-the-mean.

The comparison of diffusivity FOMs benefits from error minimization. The error in specific surface areas by BET and SAXS methods are presented in Fig. 5d. While local measurements by electron microscopy can also be used to derive surface area, ensemble methods such as BET or SAXS are preferrable for representative metrics. The present best-practices for surface area analysis include Ar-based BET and SAXS analysis with apparent-thickness. These two techniques yield similarly accurate specific surface areas. The corresponding error in diffusivity values are shown in Fig. 5e which are suitable for material ranking when best practices are used. As researchers continue to discover and test the diffusivity of new battery materials, the ability to rank these values will become increasingly important in terms of correlating material structures to their properties. As a preliminary demonstration, capacity-weighted diffusivities were calculated from published datasets for related materials that each exhibit second-order phase changes upon lithiation (Table 2).[21,33,61,62] Previously noted diffusivity trends with block size and Ta/Nb replacement are apparent in the D_{Qav} values which remain commensurate to the underlying $D_{\text{i}}(V)$ values as expected.[21,33] Such ranking benefits from both a comprehensive diffusivity FOM and error-minimization with best-practices for surface area analysis.

Table 2 Capacity-weighted diffusivities were calculated from published datasets with technical methods and errors noted

Material	Electrochemical technique	Diffusion length assessment (error)	D_{Qav} ($m^2\ s^{-1}$)	Diffusivity error[a]	Reference
$Nb_{16}W_5O_{55}$	PITT	SEM[b] (2.4%)	1.35×10^{-16}	4.8%	21
$Nb_{14}W_3O_{44}$	PITT	SEM[b] (2.5%)	7.29×10^{-17}	5.0%	21
$Nb_{12}WO_{33}$	PITT	SEM[b] (1.8%)	5.02×10^{-17}	3.6%	21
$Ta_{12}MoO_{33}$	ICI	SAXS (5.1%)	7.63×10^{-18}	10.2%	33
T-Nb_2O_5	EIS	N_2 BET[c] (~20%)	7.06×10^{-18}	~40%	61
$Nb_{12}MoO_{33}$	ICI	SAXS (0.83%)	6.30×10^{-18}	1.66%	33
$TiNb_2O_7$	GITT	N_2 BET[c] (~20%)	5.54×10^{-18}	~40%	62

[a] Diffusivity error propagated from diffusion length error. [b] Diffusion length error calculated as the error-of-the-mean reported value. [c] Diffusion length error estimated based on ref. 47–49.

Conclusion

Battery materials with improved ionic and electronic transport are necessary for a future with fast-charging anodes. Most transport metrics are reported over a range of voltages with varied reporting methods. For first order phase change materials, most redox occurs at one voltage, allowing that voltage to appropriately represent the material's transport characteristics. However, second-order phase change materials exhibit redox over a broad range of voltages where alternative reporting methods are needed to capture the range of behaviors. Using a capacity-weighted average, the voltage dependent data is combined into one representative value. Capacity-weighted figures-of-merit (D_{Qav}) can be derived using a weighing function based on differential capacity (dQ/dV). In addition, galvanostatic techniques supply transport values with even capacity-weighting such that the mean value (D_{Tav}) is inherently capacity-weighted. Both FOMs are equivalent mathematically, but D_{Tav} avoids data smoothing and interpolation necessary for the dQ/dV approach. Computational simulation of diffusivity can also be tailored to a capacity-weighted figures-of-merit. Uncertainty associated with diffusivity is heavily influenced by surface area error due to its second-power dependence. Using best-practice BET or SAXS methods can reduce the diffusivity error from ~40% to ~2%. This collection of perspectives improves material comparisons necessary for performance-ranking and understanding structure–property relationships.

Data availability

Data for this perspective, including Sample A's and Sample B's corrected open circuit potential (E_{OC}), ICI diffusivity, ICI resistance, and ICI diffusion resistance, are available at Open Science Framework at **https://osf.io/6q2rh/?view_only=5560214975354f9fbb043a79b57918c9**.

Conflicts of interest

The authors declare no conflict of interest.

Acknowledgements

CJ S., C. S., and M. S. acknowledge DOE support (DE-SC0023377). This work made use of the South Carolina SAXS Collaborative.

References

1 J. Ma, Y. Li, N. S. Grundish, J. B. Goodenough, Y. Chen, L. Guo, Z. Peng, X. Qi, F. Yang, L. Qie, C.-A. Wang, B. Huang, Z. Huang, L. Chen, D. Su, G. Wang, X. Peng, Z. Chen, J. Yang, S. He, X. Zhang, H. Yu, C. Fu, M. Jiang, W. Deng, C.-F. Sun, Q. Pan, Y. Tang, X. Li, X. Ji, F. Wan, Z. Niu, F. Lian, C. Wang, G. G. Wallace, M. Fan, Q. Meng, S. Xin, Y.-G. Guo and L.-J. Wan, *J. Phys. D: Appl. Phys.*, 2021, **54**, 183001.
2 C. Heubner, K. Nikolowski, S. Reuber, M. Schneider, M. Wolter and A. Michaelis, *Batteries Supercaps*, 2021, **4**, 268–285.
3 M. E. Houck, A. S. Groombridge, M. F. L. D. Volder and A. M. Boies, *Cell Rep. Phys. Sci.*, 2023, **4**, 101410.
4 R. Borah, F. R. Hughson, J. Johnston and T. Nann, *Mater. Today Adv.*, 2020, **6**, 100046.
5 A. Vu, Y. Qian and A. Stein, *Adv. Energy Mater.*, 2012, **2**, 1056–1085.
6 C. Sturgill, I. Milisavljevic, S. C. Wechsler, M. Muhit, H.-C. Zur Loye, S. Misture and M. Stefik, *Chem. Mater.*, 2024, Submitted.
7 Y.-C. Chien, H. Liu, A. S. Menon, W. R. Brant, D. Brandell and M. J. Lacey, *Nat. Commun.*, 2023, **14**, 2289.
8 L. Yin, Z. Geng, Y.-C. Chien, T. Thiringer, M. J. Lacey, A. M. Andersson and D. Brandell, *Electrochim. Acta*, 2022, **427**, 140888.
9 W. Weppner and R. A. Huggins, *J. Electrochem. Soc.*, 1977, **124**, 1569.
10 J. Kim, S. Park, S. Hwang and W.-S. Yoon, *J. Electrochem. Sci. Technol.*, 2021, **13**, 19–31.
11 M. D. Levi, E. Markevich and D. Aurbach, *Electrochim. Acta*, 2005, **51**, 98–110.
12 J. Li, F. Yang, X. Xiao, M. W. Verbrugge and Y.-T. Cheng, *Electrochim. Acta*, 2012, **75**, 56–61.
13 F. Mansfeld and U. Bertocci, *Electrochemical Corrosion Testing, ASTM International100 Barr Harbor Drive, PO Box C700*, West Conshohocken, PA, 1981, pp. 1–411.
14 M. El-Azazy, M. Min and P. Annus, *Electrochemical Impedance Spectroscopy*, BoD – Books on Demand, 2020.
15 C. Deng and W. Lu, *J. Power Sources*, 2020, **473**, 228613.
16 M. Wang, Z. Yao, Q. Li, Y. Hu, X. Yin, A. Chen, X. Lu, J. Zhang and Y. Zhao, *J. Energy Chem.*, 2022, **69**, 601–611.
17 X. Jin, Y. Deng, H. Tian, M. Zhou, W. Tang, H. Dong, X. Zhang and R. Liu, *Green Energy Environ.*, 2024, **9**, 1257–1266.
18 J. L. Allen, X. Ren, C. K. Nguyen, D. C. Horn, H. H. Sun and D. T. Tran, *ChemElectroChem*, 2023, **10**, e202300267.
19 B. Babu and M. M. Shaijumon, *Electrochim. Acta*, 2020, **345**, 136208.
20 J. Zheng, R. Xia, C. Sun, N. Yaqoob, Q. Qiu, L. Zhong, Y. Li, P. Kaghazchi, K. Zhao, J. E. ten Elshof and M. Huijben, *Small*, 2023, **19**, 2301967.
21 L. D. Salzer, B. Diamond, K. Nieto, R. C. Evans, A. L. Prieto and J. B. Sambur, *ACS Appl. Energy Mater.*, 2023, **6**, 1685–1691.
22 W. Van Den Bergh and M. Stefik, *Adv. Funct. Mater.*, 2022, **32**, 2204126.
23 Y. Gogotsi and R. M. Penner, *ACS Nano*, 2018, **12**, 2081–2083.
24 S. C. Wechsler, A. Gregg and M. Stefik, *Adv. Funct. Mater.*, 2024, **34**, 2312839.
25 E. Lim, C. Jo, H. Kim, M.-H. Kim, Y. Mun, J. Chun, Y. Ye, J. Hwang, K.-S. Ha, K. C. Roh, K. Kang, S. Yoon and J. Lee, *ACS Nano*, 2015, **9**, 7497–7505.
26 K. J. Griffith, I. D. Seymour, M. A. Hope, M. M. Butala, L. K. Lamontagne, M. B. Preefer, C. P. Koçer,

G. Henkelman, A. J. Morris, M. J. Cliffe, S. E. Dutton and C. P. Grey, *J. Am. Chem. Soc.*, 2019, **141**, 16706–16725.
27 A. A. Voskanyan, K. Jayanthi and A. Navrotsky, *Chem. Mater.*, 2022, **34**, 10311–10319.
28 S. Sun, L. Qin, Y. Sun and C. Guo, *Energy Fuels*, 2024, **38**, 2463–2471.
29 R. Tao, G. Yang, E. C. Self, J. Liang, J. R. Dunlap, S. Men, C.-L. Do-Thanh, J. Liu, Y. Zhang, S. Zhao, H. Lyu, A. P. Sokolov, J. Nanda, X.-G. Sun and S. Dai, *Small*, 2020, **16**, 2001884.
30 Y. Yang and J. Zhao, *Adv. Sci.*, 2021, **8**, 2004855.
31 K. J. Griffith, K. M. Wiaderek, G. Cibin, L. E. Marbella and C. P. Grey, *Nature*, 2018, **559**, 556–563.
32 X. Zhu, J. Xu, Y. Luo, Q. Fu, G. Liang, L. Luo, Y. Chen, C. Lin and X. S. Zhao, *J. Mater. Chem. A*, 2019, **7**, 6522–6532.
33 M. A. A. Muhit, S. C. Wechsler, Z. J. L. Bare, C. Sturgill, N. Keerthisinghe, M. A. Grasser, G. Morrison, C. Sutton, M. Stefik and H.-C. zur Loye, *Chem. Mater.*, 2024, **36**, 10626–10639.
34 D. D. Robertson, H. Cumberbatch, D. J. Pe, Y. Yao and S. H. Tolbert, *ACS Nano*, 2024, **18**, 996–1012.
35 J. F. Liu, Y. He, W. Chen, G. Q. Zhang, Y. W. Zeng, T. Kikegawa and J. Z. Jiang, *J. Phys. Chem. C*, 2007, **111**, 2–5.
36 W. Van Den Bergh, S. Wechsler, H. N. Lokupitiya, L. Jarocha, K. Kim, J. Chapman, K. E. Kweon, B. C. Wood, S. Heald and M. Stefik, *Batteries Supercaps*, 2022, **5**, e202200056.
37 T. Brezesinski, J. Wang, S. H. Tolbert and B. Dunn, *Nat. Mater.*, 2010, **9**, 146–151.
38 C. P. Koçer, K. J. Griffith, C. P. Grey and A. J. Morris, *J. Am. Chem. Soc.*, 2019, **141**, 15121–15134.
39 C. P. Koçer, K. J. Griffith, C. P. Grey and A. J. Morris, *Chem. Mater.*, 2020, **32**, 3980–3989.
40 A. Van der Ven, Z. Deng, S. Banerjee and S. P. Ong, *Chem. Rev.*, 2020, **120**, 6977–7019.
41 I. Batatia, P. Benner, Y. Chiang, A. M. Elena, D. P. Kovács, J. Riebesell, X. R. Advincula, M. Asta, M. Avaylon, W. J. Baldwin, F. Berger, N. Bernstein, A. Bhowmik, S. M. Blau, V. Cărare, J. P. Darby, S. De, F. Della Pia, V. L. Deringer, R. Elijošius, Z. El-Machachi, F. Falcioni, E. Fako, A. C. Ferrari, A. Genreith-Schriever, J. George, R. E. A. Goodall, C. P. Grey, P. Grigorev, S. Han, W. Handley, H. H. Heenen, K. Hermansson, C. Holm, J. Jaafar, S. Hofmann, K. S. Jakob, H. Jung, V. Kapil, A. D. Kaplan, N. Karimitari, J. R. Kermode, N. Kroupa, J. Kullgren, M. C. Kuner, D. Kuryla, G. Liepuoniute, J. T. Margraf, I.-B. Magdău, A. Michaelides, J. H. Moore, A. A. Naik, S. P. Niblett, S. W. Norwood, N. O'Neill, C. Ortner, K. A. Persson, K. Reuter, A. S. Rosen, L. L. Schaaf, C. Schran, B. X. Shi, E. Sivonxay, T. K. Stenczel, V. Svahn, C. Sutton, T. D. Swinburne, J. Tilly, C. van der Oord, E. Varga-Umbrich, T. Vegge, M. Vondrák, Y. Wang, W. C. Witt, F. Zills and G. Csányi, *arXiv*, 2024, preprint, arXiv:2401.00096, DOI: **10.48550/arXiv.2401.00096**.
42 C. Chen and S. P. Ong, *Nat. Comput. Sci.*, 2022, **2**, 718–728.
43 B. Deng, P. Zhong, K. Jun, J. Riebesell, K. Han, C. J. Bartel and G. Ceder, *Nat. Mach. Intell.*, 2023, **5**, 1031–1041.
44 ECS News: Understanding and Validating Potentiostat DC Accuracy. **https://www.electrochem.org/ecsnews/understanding-and-validating-potentiostat-dc-accuracy/** (accessed 2024-07-17).
45 S. D. Kang and W. C. Chueh, *J. Electrochem. Soc.*, 2021, **168**, 120504.
46 S. D. Kang, J. J. Kuo, N. Kapate, J. Hong, J. Park and W. C. Chueh, *J. Electrochem. Soc.*, 2021, **168**, 120503.
47 M. Thommes, K. Kaneko, A. V. Neimark, J. P. Olivier, F. Rodriguez-Reinoso, J. Rouquerol and K. S. W. Sing, *Pure Appl. Chem.*, 2015, **87**, 1051–1069.
48 C. Schlumberger, C. Scherdel, M. Kriesten, P. Leicht, A. Keilbach, H. Ehmann, P. Kotnik, G. Reichenauer and M. Thommes, *Microporous Mesoporous Mater.*, 2022, **329**, 111554.
49 J. W. M. Osterrieth, J. Rampersad, D. Madden, N. Rampal, L. Skoric, B. Connolly, M. D. Allendorf, V. Stavila, J. L. Snider, R. Ameloot, J. Marreiros, C. Ania, D. Azevedo, E. Vilarrasa-Garcia, B. F. Santos, X.-H. Bu, Z. Chang, H. Bunzen, N. R. Champness, S. L. Griffin, B. Chen, R.-B. Lin, B. Coasne, S. Cohen, J. C. Moreton, Y. J. Colón, L. Chen, R. Clowes, F.-X. Coudert, Y. Cui, B. Hou, D. M. D'Alessandro, P. W. Doheny, M. Dincă, C. Sun, C. Doonan, M. T. Huxley, J. D. Evans, P. Falcaro, R. Ricco, O. Farha, K. B. Idrees, T. Islamoglu, P. Feng, H. Yang, R. S. Forgan, D. Bara, S. Furukawa, E. Sanchez, J. Gascon, S. Telalović, S. K. Ghosh, S. Mukherjee, M. R. Hill, M. M. Sadiq, P. Horcajada, P. Salcedo-Abraira, K. Kaneko, R. Kukobat, J. Kenvin, S. Keskin, S. Kitagawa, K. Otake, R. P. Lively, S. J. A. DeWitt, P. Llewellyn, B. V. Lotsch, S. T. Emmerling, A. M. Pütz, C. Martí-Gastaldo, N. M. Padial, J. García-Martínez, N. Linares, D. Maspoch, J. A. Suárez del Pino, P. Moghadam, R. Oktavian, R. E. Morris, P. S. Wheatley, J. Navarro, C. Petit, D. Danaci, M. J. Rosseinsky, A. P. Katsoulidis, M. Schröder, X. Han, S. Yang, C. Serre, G. Mouchaham, D. S. Sholl, R. Thyagarajan, D. Siderius, R. Q. Snurr, R. B. Goncalves, S. Telfer, S. J. Lee, V. P. Ting, J. L. Rowlandson, T. Uemura, T. Iiyuka, M. A. van der Veen, D. Rega, V. Van Speybroeck, S. M. J. Rogge, A. Lamaire, K. S. Walton, L. W. Bingel, S. Wuttke, J. Andreo, O. Yaghi, B. Zhang, C. T. Yavuz, T. S. Nguyen, F. Zamora, C. Montoro, H. Zhou, A. Kirchon and D. Fairen-Jimenez, *Adv. Mater.*, 2022, **34**, 2201502.
50 Y. Shen, K. Schäfer, S. Brandt, K. Li and W.-C. Cheng, *Microporous Mesoporous Mater.*, 2022, **344**, 112210.
51 O. Spalla, S. Lyonnard and F. Testard, *J. Appl. Crystallogr.*, 2003, **36**, 338–347.
52 Z. Lu, D. Rébiscoul, T. Narayanan and T. Zemb, *J. Appl. Crystallogr.*, 2022, **55**, 1154–1163.
53 G. Porod, *Kolloid-Z.*, 1951, **124**, 83–114.
54 NIST: Scattering Length Density Calculator. **https://www.ncnr.nist.gov/resources/activation/**(accessed 2024-04-19).
55 NIST: X-ray Form Factor, Attenuation, and Scattering Tables. **https://physics.nist.gov/PhysRefData/FFast/html/form.html** (accessed 2024-04-19).

56 South Carolina SAXS Collaborative (SCSC). **http://saxs.sc.edu** (accessed 2024-08-14).
57 Cornell High Energy Synchrotron Source (CHESS). **https://www.chess.cornell.edu/**(accessed 2024-08-14).
58 Berkeley Lab: Advanced Light Source (ALS). **https://als.lbl.gov/**(accessed 2024-08-14).
59 Argonne National Lab: Advanced Photon Source (APS). **https://www.aps.anl.gov/**(accessed 2024-08-14).
60 Stanford Synchrotron Radiation Lightsource (SSRL). **https://www-ssrl.slac.stanford.edu/**(accessed 2024-08-14).
61 M. V. Reddy, R. Jose, A. Le Viet, K. I. Ozoemena, B. V. R. Chowdari and S. Ramakrishna, *Electrochim. Acta*, 2014, **128**, 198–202.
62 F. Yu, S. Wang, R. Yekani, A. La Monaca and G. P. Demopoulos, *J. Energy Storage*, 2024, **95**, 112482.